ACS OMEGA

Article

Cite This: ACS Omega 2018, 3, 6190−6198

Polycrystalline Diamond Thin-Film Waveguides for Mid-Infrared Evanescent Field Sensors

Julian Haas,[†,‡] Ernesto Vargas Catalán,[‡] Pierre Piron,[‡] Fredrik Nikolajeff,[‡,§] Lars Österlund,[‡,§] Mikael Karlsson,[*,‡,§] and Boris Mizaikoff[*,†]

[†]Institute of Analytical and Bioanalytical Chemistry, Ulm University, Albert-Einstein-Allee 11, 89081 Ulm, Germany

[‡]Department of Engineering Sciences, Uppsala University, Box 534, SE-75121 Uppsala, Sweden

[§]Molecular Fingerprint Sweden AB, Eksätravägen 130, SE-756 55 Uppsala, Sweden

ABSTRACT: Photonic design and optimization of thin-film polycrystalline diamond waveguides are shown, serving as advanced evanescent field transducers in the mid-infrared fingerprint regime (2000−909 cm^{-1}; 5−11 μm). Design constraints inherent to optical/system considerations and the material were implemented in a finite element method (FEM)-based simulation method that allowed three-dimensional modeling of the overall structure. Thus, lateral mode confinement, attenuation in the direction of radiation propagation, and physical resilience were evaluated. In a final step, the designed structures were fabricated, and their utility in combination with a broadly tunable external cavity quantum cascade laser for chemical sensing of a liquid phase analyte was demonstrated.

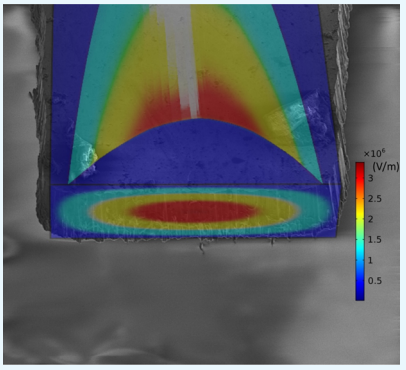

1. INTRODUCTION

Diamond is among the most durable materials available nowadays applied in a variety of mechanically and chemically demanding application scenarios. Bulk crystals have been used in long-lasting micromechanical compartments such as clock gears; as tools such as wear-resistant sharp scalpels for ocular surgery; as optical components in the X-ray, visible (vis)-optical, infrared, and THz spectral regime; and for heat management applications. Furthermore, diamond is being used as the key material in fusion research, as nuclear radiation detector or—with NV centers—in quantum physics.[1,2] Diamond thin-film coatings have gained increasing interest as ultradurable and electrically insulating coatings in microchip technology and in optical compartments deployed in outer space or defense applications.[3] In the context of mid-infrared (MIR) sensing, diamond has matured to be the material of choice in environmentally demanding sensing scenarios. Materials routinely used as infrared transparent windows for transmission experiments including calcium fluoride (CaF_2) or zinc selenide (ZnSe) are brittle, prone to scratching, and resist only a limited set of solvents. Diamond on the contrary is considered chemically highly inert, and—because of the hardness—resists physical damage of almost any kind.

Apart from analyzing thin films of liquids, attenuated total reflection (ATR) techniques allow probing MIR opaque matrices such as aqueous solutions, as well as gel-like materials and solids including ground powders, polymers, or bulk material surfaces without requiring additional sample preparation procedures [i.e., such as pressing into potassium bromide (KBr) pellets].[4,5] Again, commonly applied MIR transparent ATR crystal materials with high refractive indices such as silicon (Si), ZnSe, ZnS, chalcogenide glasses, or single-crystalline germanium (Ge) have to be handled with care. In contrast, ATR waveguides made from diamond can be utilized in the most demanding circumstances with limitations only in IR transparency in the spectral region 2200−1800 cm^{-1} (4.5−5.6 μm) because of two-phonon crystal lattice absorption features.[6] Corrosive media as well as sharp-edged solids may readily be probed using diamond ATR crystals.

Specifically, for chemical sensing in the MIR, the window 1800−600 cm^{-1} is of interest, constituting the so-called fingerprint regime, which gives rise to strong fundamental vibrational modes of inorganic and organic molecules in the condensed phase. In the gas-phase, roto-vibrational modes may be excited in this spectral window, as rotational transitions are already excited at lower energies in the far infrared. ATR spectroscopy is based on the formation of an evanescent field at the location of internal total reflections at the crystal/sample interface. Increasing the number of internal reflections leads to an increased interaction area/volume of the probing light with the analyte matrix. Besides elongating the waveguide length, reducing the thickness leads to an increased number of internal reflections. Ultimately, a uniform evanescent field surrounding the internal reflection element (IRE) is established once the geometrical dimensions are close to the supported wavelength with the IRE actually serving as a waveguide.[7]

Received: April 2, 2018
Accepted: May 22, 2018
Published: June 8, 2018

DOI: 10.1021/acsomega.8b00623
ACS Omega 2018, 3, 6190−6198

Dielectric waveguides have nowadays readily expanded from the visible and the near infrared into the MIR. Operation of thin-film waveguides made from initially bulk materials such as Ge,[8−10] Si,[11] ZnS,[12] ZnSe,[13] and chalcogenide glasses,[14,15] as well as Si-on-sapphire[16] has been reported in data transfer applications, and chem/biosensing and detection scenarios. Furthermore, more advanced materials such as gallium arsenide (GaAs)[17,18] and ternary mercury−cadmium−telluride mixtures (HgCdTe, MCT)[19] have been introduced as versatile thin-film waveguide platforms in MIR evanescent field chem/biosensors. With increasing availability, diamond has increasingly emerged as an alternative thin-film MIR waveguide material.[20,21] The fundamental utility of thin-film diamond-based transducers for chemical detection in the MIR has recently been reported.[22−24]

However, for most materials, there is a gap between their theoretical feasibility serving as MIR waveguide and their manufacturability and tailorability toward selected application scenarios. On the one hand, optical and geometrical design parameters have to be adjusted, enabling the desired wave-guiding properties, while useful processing schemes and material availability have to be ensured. Optical properties such as the refractive index (i.e., real and imaginary parts) of these materials have to be matched to confine light within the actual waveguiding photonic structure while minimizing attenuation losses of the transmitted radiation. Furthermore, adequate fabrication technologies have to be available for growing and structuring the material of choice. Last but not least, limiting factors on the choice of materials include harsh growth or structuring steps during production, whereas, for example, thermal expansion coefficients and/or chemical interactions between various material layers (e.g., substrate, adhesion layer, waveguide layer, etc.) have to be tailored to avoid delamination or buckling of the actual thin-film waveguide layer. On the other hand, the final device needs to meet an operational design that allows practical application for the desired task. Finally, evanescent field sensors have to provide sufficient structural integrity and robustness during liquid or solid analyte deposition, cleaning procedures, etc.

In the present study, we show the evaluation and optimization of polycrystalline diamond (PCD) thin-films grown at Si wafer substrates with a Si dioxide (SiO_2) optical cladding layer via finite element modeling (FEM). Suitable boundary conditions given by the material properties and technological availability were explored, and Si nitride (Si_3N_4) as an additional cladding layer was studied. Finally, the experimental application of a thin-film PCD waveguide manufactured according to the derived design rules in an evanescent field chem/biosensing scenario was shown in combination with a broadly tunable external cavity quantum cascade laser (EC-QCL) light source in the wavelength regime of 2000−909 cm^{-1} (5−11 μm), as required for analytical applications in the MIR fingerprint spectral regime.

2. RESULTS AND DISCUSSION

2.1. Growth. The first step in thin-film diamond waveguide fabrication is selecting optimized growth conditions. Besides defining the desired optical parameters, material aspects of the various layers have to be matched. In particular, lattice mismatch has to be reduced, and thermal expansion coefficients (Figure 1) have to be selected, reducing inter- and intralayer stress. Additionally, the selected substrates have to endure elevated temperatures in a hydrogen-rich atmosphere. Most commonly used MIR transparent materials such as alkali metal and silver halides or KRS-5 are susceptible to harsh growth conditions at temperatures up to 800 °C. Furthermore, the substrate should form strong carbide bonds for supporting diamond adhesion. Besides utilizing diamond itself, molybdenum and Ir/YSZ/Si[28] have been introduced as suitable substrate materials for chemical vapor deposition (CVD) of diamond bulk crystals even at single crystalline quality.[29] Si and SiO_2 have been successfully implemented as versatile substrates for nano- and microcrystalline diamond growth. Si crystallizes in a diamond lattice and in addition generates a strongly bound carbide (SiC). Furthermore, toxic materials such as lead or cadmium salts, selenides, and arsenides can be avoided using the Si technology. However, Si has a refractive index of approx. 3.4 in the MIR, which is higher than that of diamond (n_i = 2.4). Hence, an adequate cladding layer has to be inserted between the diamond film and the Si substrate. Commonly, SiO_2 is used as it is readily grown on top of Si via thermal formation or plasma-enhanced CVD prior to the diamond growth.

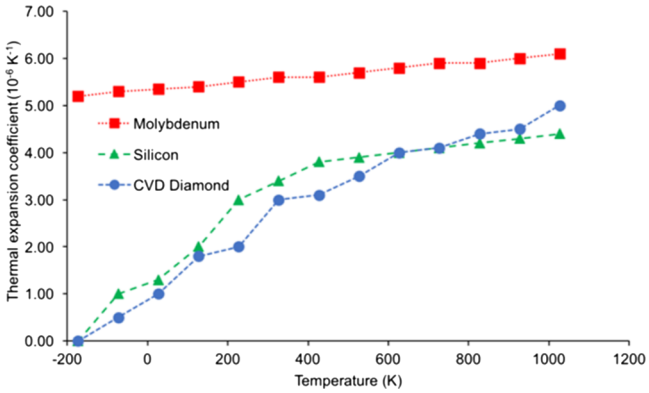

Figure 1. Thermal expansion coefficients of commonly used substrate materials for diamond deposition including CVD diamond,[30] Si,[31] and molybdenum.[32]

2.2. Structuring. In the literature, it has been shown for the example of unstructured slab waveguides fabricated from GaAs/AlGaAs that manual handling is facilitated for chip dimensions of 10 × 5 mm, while enabling highly sensitive evanescent field absorption spectroscopy via the vertically stacked waveguide structure.[33−35] However, because of the comparably low refractive index of diamond (2.4) versus GaAs (3.4), IR radiation is more weakly confined within the diamond structure, and triangular spreading along the propagation axis is much more pronounced compared to GaAs. As shown in the calculations visualized in Figure 2, after 1 cm of propagation within the waveguide structure an initial beam diameter of 6 μm results in a wave front (mode) with a full width of half-maximum (fwhm) of 1556 μm in diamond, which is about twice the fwhm in GaAs (i.e., 824 μm). Consequently, propagation losses are much more pronounced as decoupling via side facets is possible and collecting emitted radiation at the distal facet becomes more complex. Horizontal structuring of slab waveguides into waveguide strips resolves this issue, as additional air cladding limits horizontal dispersion and an increased amount of radiation efficiently collected at the outcoupling facet.

As shown in Figure 3, the derived attenuation of the diamond waveguides is high compared to the attenuation of, for example, silica fibers (~0.16 dB/km)[36] ranging from approx. 10 to 70 dB/cm. However, the combination of short transducer dimensions (i.e., 1 cm) and bright MIR light sources (i.e.,

DOI: 10.1021/acsomega.8b00623
ACS Omega 2018, 3, 6190−6198

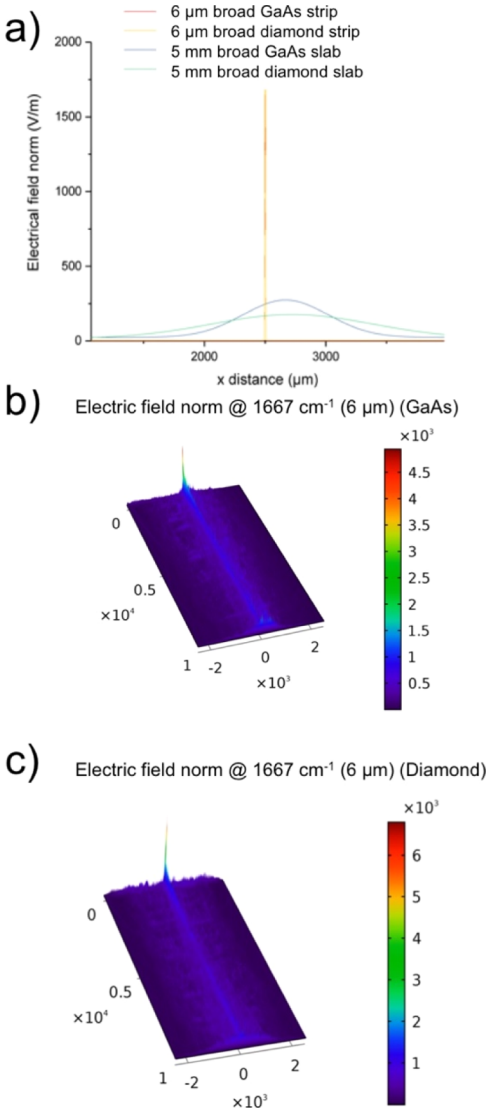

Figure 2. (a) Comparison of the fwhm of wave fronts propagated through slab waveguides (5 mm wide) and strip waveguides (6 μm wide) made from diamond and GaAs. The improved lateral wave front confinement for strip structures (dimensions in μm) is immediately evident. (b) Scattering within a GaAs slab waveguide. (c) Scattering within a diamond slab waveguide (dimensions in μm).

QCLs) with peak emission powers of up to 500 mW enables transmission characteristics through these photonic structures suitable for chem/biosensing applications. Relatively weak attenuation between 1666 and 1429 cm^{-1} (6 and 7 μm) renders these waveguides suitable for the investigation of, for example, proteins, as amide I and II bands are present within this spectral window.[22,37] Toward shorter wavelengths, the attenuation is apparently increased because of the two-phonon crystal lattice absorption feature inherent to diamond.[6] Toward longer wavelengths, differences in attenuation intensity are evident for different cladding layouts.

Considering a theoretical free-standing diamond strip, the attenuation decreases continuously, as no inherent diamond absorption features are apparent toward the longer wavelength regime. For a 6 μm thick waveguide supported by a solid cladding bottom layer made from SiO_2, the attenuation steeply increases at wavelengths >7 μm. This results from the pronounced absorption feature of the cladding layer made from SiO_2, which is centered at approx. 9.3 μm (~1100 cm^{-1}) with an absorption shoulder at 8.4 μm (~1190 cm^{-1}).

Waveguides with a thickness of 10 μm are affected by the same cladding absorption features. However, attenuation at 8 μm is only about 1/3 of the attenuation of the 6 μm thick waveguides, which is due to the decreased interaction of the propagated electric field with the cladding layer because of the confinement in a geometrically more spacious structure. Further opening of the spectral transparency window may be achieved by the addition of a Si_3N_4 film in between the SiO_2 and the diamond layer. Si_3N_4 has a pronounced infrared absorption feature at approx. 11.5 μm (870 cm^{-1}) with a small shoulder at approx. 8 μm (1250 cm^{-1}). As a consequence, the transmission window should extend up to wavelengths of 9 μm before increasing attenuation losses prohibit further transmission. The thickness of the Si_3N_4 layer was selected at 200 nm, as such thin films can be deposited largely defect-free, and the evanescent field intensity drops relatively rapidly within the cladding layer. As shown in Figure 3d for exemplary wavelengths of 1666 and 1250 cm^{-1} (6 and 8 μm), the evanescent field already drops to a value of $1/e$ after approx. 1 μm within the SiO_2 cladding layer. Hence, the interaction with the stronger absorbing n-doped Si substrate is effectively avoided. Consequently, already a thin intermediate layer between diamond and SiO_2 effectively reduces the interaction and improves the waveguiding properties.

As a tradeoff between structural support and ideal waveguiding properties, free-standing diamond waveguides supported by a frame-shaped substrate may be envisioned. Interaction with the strongly absorbing cladding layers can be reduced by reducing the thickness of that layer in a subsequent processing step after the growth. However, the structural support is likewise reduced, and the utility as an evanescent field transducer element may be limited.

Within the predefined set of suitable designs for optimized waveguiding properties, the requirements for chem/biosensing applications in terms of transducer robustness cannot be neglected. Our calculations show that free-standing single mode waveguides with the required dimensions (6 × 6 or 10 × 10 μm) are not sufficiently robust to withstand the addition of even a single water droplet with a volume of 50 μL. However, increasing the waveguide thickness to, for example, 14 μm or using a slab with, for example, 100 μm results in robust optical transducer elements, as shown in Figure 4. If the physical stress exceeds approx. 300 MPa for reduced waveguide dimensions (marked with the red line), free-standing waveguide structures are likely to break.

However, further variations of the frame design are possible such as adding a third frame leg to support the waveguides or varying the length of the waveguides and correspondingly, the free-standing segment.

Yet, more advanced designs can be considered given the boundary conditions of photonic properties and structural integrity in chem/biosensing applications. Instead of removing the supporting substrate structure completely or reducing to a frame, slots in the substrate leaving diamond membranes may be conceived. With this concept, the interfering oxide cladding can be entirely removed at the backside of the waveguide to establish an air cladding similar to free-standing waveguides, yet only in the actual waveguiding areas.

Introducing rib waveguides is a logical consequence to confine light within predefined areas, while maintaining lateral structural support. The design layout presented in Figure 8 may

DOI: 10.1021/acsomega.8b00623
ACS Omega 2018, 3, 6190−6198

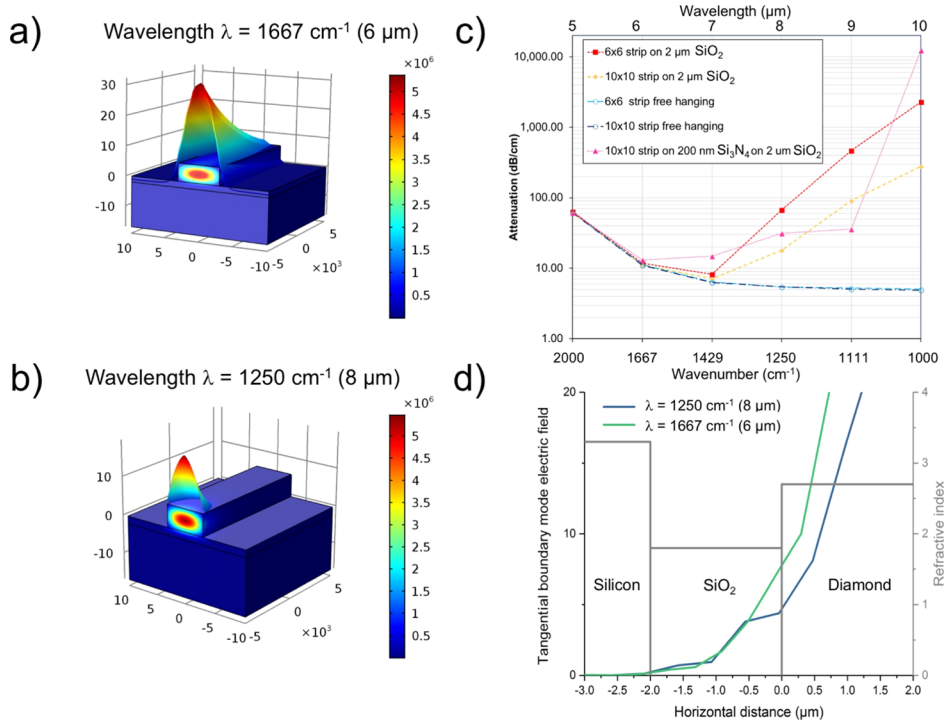

Figure 3. (a) Electric field (V/m) within a 1 cm long diamond waveguide (6 × 6 μm) at a wavelength of 6 μm. (b) Electric field (V/m) in a 1 cm long diamond waveguide (6 × 6 μm) at a wavelength of 8 μm. (c) Comparison of the calculated attenuation for different waveguide structures. Free-standing diamond waveguides show reduced attenuation toward longer wavelengths (dark and light blue). Waveguides deposited onto a SiO_2 cladding layer (red and yellow) show increased attenuation toward the SiO_2 absorption feature. An additional Si_3N_4 cladding increases the accessible spectral window toward longer wavelengths (purple). (d) Calculated penetration depth of the evanescent field emanating from a 6 μm thick diamond waveguide into a 2 μm thick SiO_2 cladding layer for the exemplary wavelengths of 6 and 8 μm.

thus be modified by adding an additional diamond slab adjacent to the initial waveguide. An exemplary permutation of potential rib designs is shown in Figure 5 for a wavelength (λ) of 6 μm altering the waveguide width (w), the slab height (r), and the waveguide height (h). The corresponding simulations show that no waveguiding is possible for $h < 4$ μm, $w < 4$ μm, and $r < 4$ μm. Slab modes are enabled though for $r > 3$ μm, which has to be avoided because the waveguiding properties, that is lateral confinement, is lost, and the waveguide would only serve as a slab structure. On the other hand, r should not be too small, as the structural robustness may increasingly be affected using thinner slab membranes. An ultimate slab height of 0 would then essentially correspond to a strip waveguide. Multiple modes appear for $w > 10$ μm, $h > 6$ μm, and $r < 3$ μm. Multimode waveguiding maintains the waveguiding properties of the transducer, however, at increased losses and with lower sensitivity affecting the overall sensor performance.[39] Calculations reveal that the targeted single-mode range is achieved at geometrical properties that are close to a fitted surface following eq 1.

$$w = 13.8 + 0.74 \cdot r - 1.31 \cdot h - 0.48 \cdot r^2 + 0.04 \cdot h^2 \quad (1)$$

2.3. Experimental Verification of the Derived Waveguide Design Rules. Transmission spectra of slab waveguides at different optimization steps reveal that the properties predicted from the theoretical calculations are indeed correct. A simple diamond slab waveguide deposited onto a SiO_2 cladding layer shows poor transmission within the MIR fingerprint window ranging from 2000 to 909 cm^{-1} (5−11 μm). Transmission is reduced by the two-phonon absorption in diamond toward the short wavelength range, as anticipated. Toward the longer wavelength regime, transmission is limited by the SiO_2 absorption. Focused ion beam (FIB) polishing of the waveguide edges results in a minor improvement of the transmitted light intensity. As suggested from the calculations, only removing the Si substrate does not result in a significant improvement of the transmission performance. This further confirms that a 2 μm cladding layer is sufficient to suppress coupling of radiation into the substrate.

Significant improvement of the transmission properties by a factor of approx. 6 is achieved, if the SiO_2 cladding layer is removed from the backside as well, and an air cladding is introduced (Figure 6).

Furthermore, the performance of a 500 μm wide and 14 μm thick free-standing PCD waveguide has been evaluated. The waveguide is supported by a Si frame with a contact length of approx. 4 mm^2. The cladding consisted of 2 μm SiO_2 and 200 nm of Si_3N_3 in between the Si substrate and the diamond waveguide layer. The SiO_2 cladding layer was removed from the free-standing areas of the waveguide. Again, the obtained spectra show little transmission toward the two-phonon absorption feature around 2000 cm^{-1} (5 μm) and toward the SiO_2 absorption feature around 1100 cm^{-1} (9 μm) (Figure 7).

To evaluate the fundamental suitability for chem/bioevanescent field sensing applications, exemplarily a 50 μL water droplet was deposited at the waveguide surface, and the background spectrum (I_0) was recorded. Subsequently, defined volumes of *N*-*N*-dimethylformamide (DMF) in water were added as droplets to the waveguide surface, and sample spectra (I) were recorded. The final absorbance spectra (A) were calculated according to $A = -\log(I/I_0)$. Using the 3σ noise criterion, a limit of detection of approx. 5 vol % was derived.

DOI: 10.1021/acsomega.8b00623
ACS Omega 2018, 3, 6190−6198

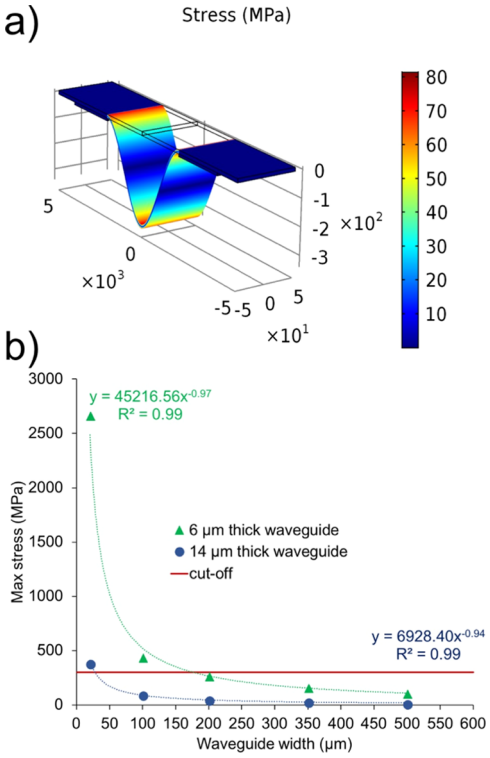

Figure 4. (a) Structural stress on a 14 × 100 μm free-standing diamond waveguide with the addition of one droplet of water at the surface (dimensions in μm). (b) Summary of the structural stress for different waveguide widths with 6 and 14 μm thickness. The red line represents the maximum stress level, which these diamond strips are most likely to withstand. Smaller geometric dimensions (i.e., area above the red line) will result in higher stress levels, and the waveguides will break according to literature values.[38]

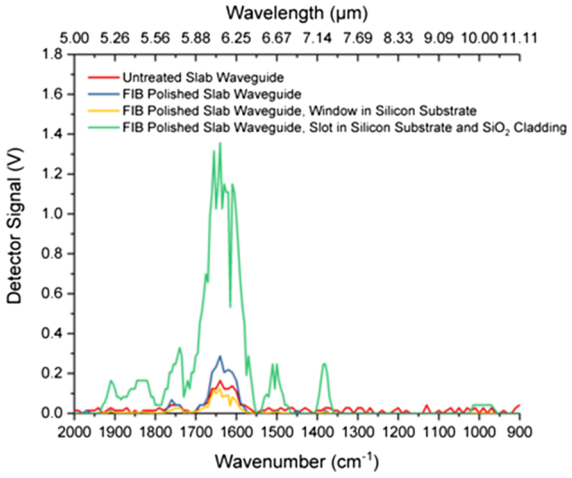

Figure 6. Experimental evaluation of the transmission behavior of diamond waveguides deposited onto a SiO_2 cladding at different stages of the manufacturing process. Untreated (red line), FIB polished (blue line), and waveguides with the Si substrate removed from the backside (yellow line) show poor transmission in the MIR fingerprint regime, whereas partly removing the SiO_2 cladding results in improved transmission. However, inherent diamond absorptions toward 2000 cm^{-1} (5 μm) and SiO_2 absorptions toward 1100 cm^{-1} (9 μm) remain clearly limiting.

Further noise reduction can be achieved by averaging an increased number of scans or applying smoothing algorithms to improve the limits of detection during future experiments.

3. CONCLUSIONS

Fundamental design considerations for the implementation of PCD waveguides serving as MIR evanescent field transducers in chem/biosensing applications have been theoretically modeled and experimentally verified in this study. Boundary conditions

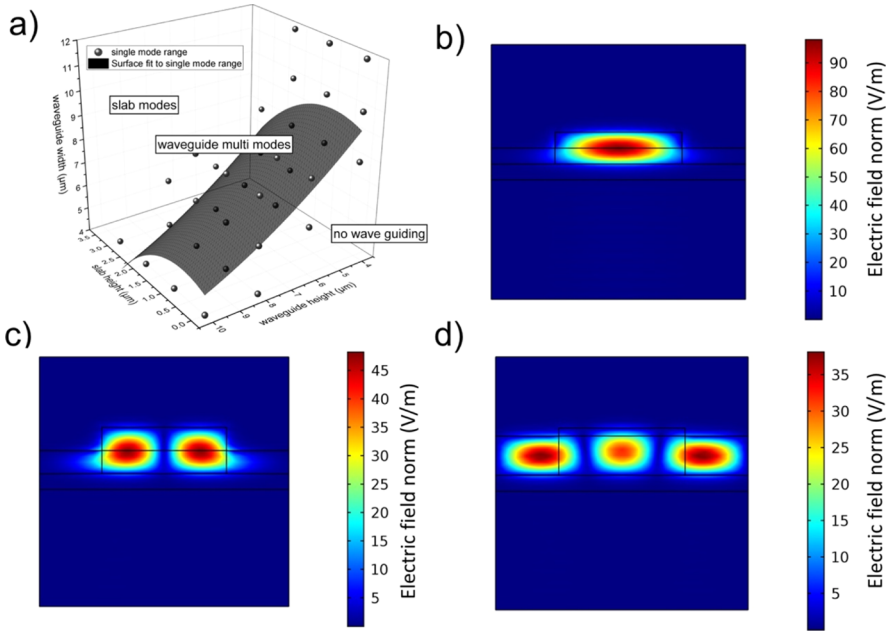

Figure 5. (a) Surface fit of single-mode regimes of a diamond rib waveguide on top of a SiO_2 cladding layer in air at a wavelength of 6 μm. (b) Calculated mode confinement for single-mode propagation via a 10 μm wide and 4 μm high waveguide with a slab height of 2 μm. (c) Calculated modes for multi-mode waveguiding within a 10 μm wide and 6 μm high waveguide with a slab height of 3 μm. (d) Calculated mode behavior for a 10 μm wide and 6 μm high waveguide with a slab height of 5 μm revealing the loss of lateral mode confinement.

DOI: 10.1021/acsomega.8b00623
ACS Omega 2018, 3, 6190−6198

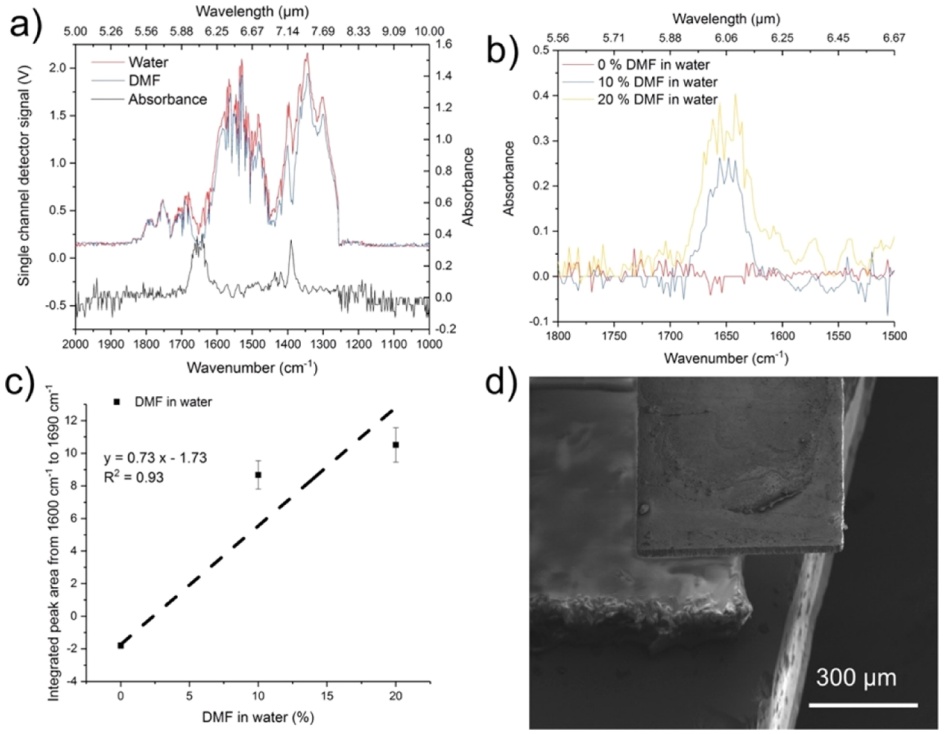

Figure 7. (a) QCL single channel and absorbance spectra of DMF in H_2O using a free-standing PCD waveguide. (b) Evaluation of the C═O absorption feature[40] of DMF at approx. 6.06 μm (1650 cm^{-1}). (c) Calibration of the DMF concentration in H_2O derived from the spectra shown in (b); negative integrals result from noise. (d) Scanning electron microscope image of the free-standing in-coupling facet of the PCD waveguide with the recessed Si frame in the background.

Table 1. Refractive Indices of the Applied Materials at Different Relevant Wavelengths (λ) in the MIR

	refractive index (real and imaginary parts)									
	air		diamond[6]		SiO_2[41]		10^{17} (cm^{-3}) n-doped Si[42,43]		Si nitride (Si_3N_4)[41]	
λ (μm)	n	k	n	k	n	k	n	k	n	k
5	1	0	2.4091	0.000553	1.3475	0.000760	3.4225	0.000279	2.3307	0.004450
6	1	0	2.4214	0.000119	1.2713	0.001606	3.4207	0.000478	2.2236	0.032326
7	1	0	2.4054	0.000785	1.1145	0.004303	3.4196	0.000836	2.1086	0.127140
8	1	0	2.3971	0.000078	0.5139	0.272730	3.4189	0.001273	2.0014	0.234300
9	1	0	2.3868	0.000081	0.5948	1.767500	3.4184	0.001432	1.7428	0.405280
10	1	0	2.3765	0.000086	2.8118	0.532170	3.4181	0.002387	1.6270	1.154100
11	1	0	2.3762	0.000091	1.9423	0.046344	3.4178	0.003501	2.2413	1.713300

derived from the material properties including potential decomposition under harsh manufacturing and experimental conditions or matching refractive indices required for establishing dielectric waveguides have been examined. FEM-based calculations have been confirmed as a versatile tool for the optimization of optical design parameters, while taking material properties as constraints into account. The resulting photonic design considerations have been aligned with mechanical demands in chem/biosensing scenarios, enabling the integration of PCD photonic structures into practically useful optical sensor devices. The addition of an additional intermediate Si_3N_4 cladding layer has been found to be beneficial to expand the accessible spectral window further into the long wavelength region. Further optimization of the respective cladding materials may lead to additional improvements of the waveguiding properties of the presented waveguide platform because of lower losses and a broader accessible spectral window.

Finally, the designed waveguide structures were actually fabricated and their function as transducer in chem/biosensors experimentally verified. For that purpose, thin-film PCD waveguides were combined with EC-QCLs for the analysis of liquid phase samples. The spectral behavior and limitations predicted by the preceding calculations have thereby been experimentally confirmed. Hence, the design rules derived in the present study may be adapted to other waveguide material systems during future investigations.

Last but not least, more sophisticated waveguide geometries including ring/disk/racetrack resonators or optical couplers may be implemented in the same model toward further enhancing the sensitivity of on-chip MIR photonics.

4. METHODS

4.1. Modeling of the Optical Properties. Optimization of the waveguide properties has been performed via the frequency domain module for two-dimensional modeling and with the beam envelope method for three-dimensional

DOI: 10.1021/acsomega.8b00623
ACS Omega 2018, 3, 6190−6198

modeling, with both included in the electromagnetic waves modules of the COMSOL Multiphysics software package (version 5.2a, COMSOL Multiphysics GmbH). Diamond waveguides on SiO_2 on an optional Si_3N_4 cladding layer and on a heavily n-doped Si substrate with an upper air cladding for a total waveguide length of 1 cm were modeled using the material properties summarized in Table 1 and the geometric design parameters illustrated in Figure 8.

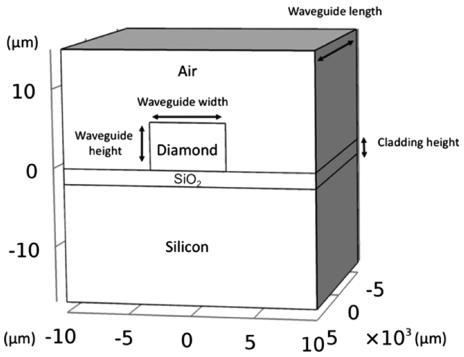

Figure 8. Geometric dimensions of the modeled diamond waveguides deposited onto a SiO_2 cladding layer and onto a heavily n-doped Si substrate. Optionally, a second cladding layer (Si_3N_4) was introduced in between the diamond and the SiO_2 layer or a diamond slab was added alongside the diamond strip. For modeling free-standing waveguide structures, the properties of the SiO_2 and the Si layers were set equal to those of the air cladding.

4.2. Modeling of the Mechanical Properties. The COMSOL Multiphysics structural mechanics module has been used to derive structural stress of free-standing waveguides of 1 cm length at a variable width of 20, 100, 200, 350, and 500 μm and at a thickness of 6 and 14 μm. Structural support was modeled via a 2 mm wide frame recessed by 1 mm from each end facet. The resulting bending forces were derived from the applied weight of a 50 μL water droplet inducing a downward-directed force of 0.491 mN. For the calculations, a diamond density of 3515 kg/m^3, Young's modulus of 1050 GPa, and Poisson's ratio of 0.1 were used (Table 2).[25]

Table 2. Properties of CVD Diamond[25,26]

crystal structure	diamond cubic
thermal expansion coefficient @ 300 K	1.0×10^{-6} K^{-1}
Young's modulus	1050 GPa
resistivity (undoped)	10^{13}–10^{16} Ω cm
resistivity (boron-doped)[27]	0.1 Ω cm
Vickers hardness	98 GPa
transparent area	225 nm to THz (lattice absorption ≈ 5 μm)
thermal conductivity	>1800 W/m K
band gap	5.45 eV
refractive index @ 6 μm	2.38

4.3. Fabrication of Diamond Waveguide Structures for Application in MIR Sensing. Thin diamond films were purchased from Diamond Materials GmbH (Freiburg, Germany). As a substrate, highly n-doped Si wafers were used. The doping level ensures that the Si substrate is opaque in the MIR because of strong free-carrier absorption. The Si bulk wafer prevented potential bending or buckling of the entire structure because of high layer strains, which may arise during the diamond growth process. On top of the Si substrate, a 2 μm SiO_2 cladding layer was thermally grown. Optionally, another 200 nm of Si_3N_4 was deposited on top of the SiO_2 layer. Then, thin-film PCD of optical grade was grown at various thicknesses via CVD. After successful growth, the Si substrate was polished from the backside until the Si layer was thinned to approx. 500 μm. Afterward, the diamond layer was polished to obtain a smooth surface (arithmetic average roughness R_a < 10 nm), and the wafer was diced into 1 × 1 cm segments. The diced chips were used for structuring free-standing waveguides. For slab waveguides, the dices were further cleaved into 5 × 10 mm segments in an optional next step. Afterward, the diamond layer was structured via a dry etching protocol based on Ar/O_2.[44−46] Next, the chips were flipped by 180°, and the backside Si material was removed via etching using a standard Bosch process for establishing slots, frames, or membranes.[24] In a last step, the chips were dipped into a buffered hydrogen fluoride solution to remove residual SiO_2 at exposed areas. Thus prepared diamond waveguides were further optimized via water-vapor-assisted FIB milling for obtaining smooth in- and out-coupling facets. Rayleigh scattering at nanoscale grain boundaries is negligible within the waveguide structure. However, end facets may be significantly rougher, giving rise to substantial in- and out-coupling losses by scattering (Figure 9).

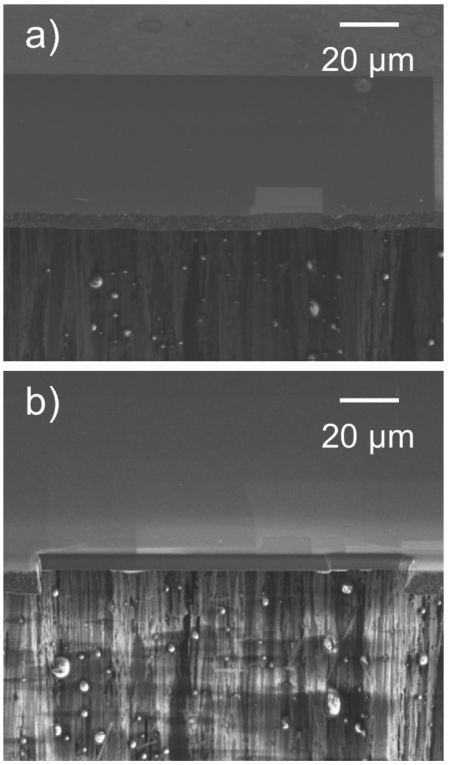

Figure 9. (a) PCD end facet before FIB polishing and (b) PCD end facet after water vapor-assisted FIB milling.

4.4. Experimental Setup. The experimental setup used for the evaluation of the PCD waveguides as the IR transducer was based on a broadly tunable EC-QCL system (MIRcat, Daylight Solutions, San Diego, CA, USA). This system comprises four individual QCLs optically coupled into one collimated output beam. The laser system covers a spectral range of 2020−890

DOI: 10.1021/acsomega.8b00623
ACS Omega 2018, 3, 6190−6198

cm^{-1} (4.95−11.24 μm) and provides approx. 500 mW of peak output power at the center wavelength of each parabolic emission curve of any particular laser chip. The laser was operated in the pulsed mode with a pulse width of 400 ns and at a repetition rate of 100 kHz. The laser head was thermoelectrically cooled (TEC) to 17 °C. The laser head emitted 100:1 vertically polarized radiation within a collimated beam, which was focused via a ZnSe lens (focal length 25 mm) onto the end facet of the PCD waveguide. Radiation at the distal end of the waveguide was collected via a second ZnSe lens (focal length, 25 mm) and subsequently focused on a detector using a third ZnSe lens (focal length, 12.7 mm). Additional apertures between the laser and the first lens, and between the second and third lens, allowed further beam shaping and intensity control (Figure 10). The detector

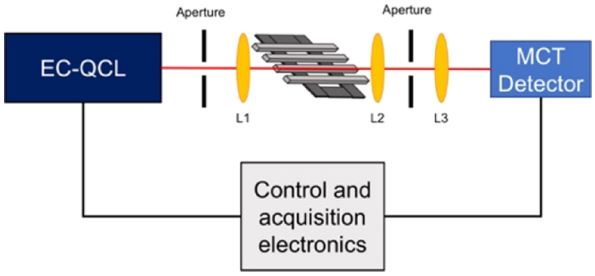

Figure 10. Schematic of the experimental setup comprising an EC-QCL, a TEC-cooled MCT detector, beam shaping apertures, and three ZnSe lenses (L1, L2, L3) along with electronics for system control and data acquisition. The actual PCD waveguide sample is located between L1 and L2 and was adjustable within the beam path in the *x*,*y*,*z*-position.

(PVMI-4TE 12 PIP-PC 200-M-F-M4, Vigo System S.A., Ozarow Mazowiecki, Poland) was based on a TEC MCT chip optically immersed into a GaAs hypersphere, which was optimized for detection at a wavelength of 10.6 μm. Data acquisition was performed via a National Instruments PC oscilloscope (NI PXIe-5114 125 MHz, 250 MS/s, 8-bit), which was operated using a LabVIEW (LabVIEW 2016) script. The script was based on tuning the QCL emission wavelength at 1 cm^{-1} increments.

AUTHOR INFORMATION

Corresponding Authors

*E-mail: mikael.karlsson@angstrom.uu.se (M.K.).
*E-mail: boris.mizaikoff@uni-ulm.de (B.M.).

ORCID

Julian Haas: 0000-0001-9378-8922
Boris Mizaikoff: 0000-0002-5583-7962

Author Contributions

All authors have given approval to the final version of the manuscript.

Notes

The authors declare no competing financial interest.

ACKNOWLEDGMENTS

The authors acknowledge the Focused Ion Beam Center UUlm (supported by FEI Company, Eindhoven, The Netherlands), the German Science Foundation (no. INST40/385-F1UG), and the Struktur-und Innovationsfonds Baden-Württemberg for assistance with device prototyping and material characterization. Furthermore, the Kompetenznetz Funktionelle Nanotrukturen (Baden-Wuerttemberg Stiftung, Germany), Carl Trygger Foundation, the Swedish Research Council (VR) project 621-2014-5959, and the Uppsala Berzelii Technology Centre for Neurodiagnostics are thanked for support of this study. The authors wish to thank the Horizon 2020 Framework Programme of the European Union for funding within the MSCA RISE Project TROPSENSE. The computations were performed on resources provided by SNIC through the Uppsala Multidisciplinary Center for Advanced Computational Science (UPPMAX) under Project SNIC 2016-7-107.

REFERENCES

(1) Bradac, C.; Gaebel, T.; Rabeau, J. R. Nitrogen-Vacancy Color Centers in Diamond: Properties, Synthesis, and Applications. *Optical Engineering of Diamond*; Wiley-VCH Verlag GmbH & Co. KGaA: Weinheim, Germany, 2013; pp 143−175.
(2) Gicquel, A.; Hassouni, K.; Silva, F.; Achard, J. CVD Diamond Films: From Growth to Applications. *Curr. Appl. Phys.* **2001**, *1*, 479−496.
(3) Li, J.; He, D.; Guo, W.; Zhang, J.; Sun, Y.; Lei, Q.; Gao, X. Nanocrystalline Diamond Thin Films As Infrared Optical Protective Coatings. *Int. J. Mod. Phys. B* **2002**, *16*, 1013−1017.
(4) Müller, C. M.; Pejcic, B.; Esteban, L.; Piane, C. D.; Raven, M.; Mizaikoff, B. Infrared Attenuated Total Reflectance Spectroscopy: An Innovative Strategy for Analyzing Mineral Components in Energy Relevant Systems. *Sci. Rep.* **2014**, *4*, 6764.
(5) Kos, G.; Sieger, M.; McMullin, D.; Zahradnik, C.; Sulyok, M.; Öner, T.; Mizaikoff, B.; Krska, R. A Novel Chemometric Classification for FTIR Spectra of Mycotoxin-Contaminated Maize and Peanuts at Regulatory Limits. *Food Addit. Contam., Part A* **2016**, *33*, 1596−1607.
(6) Dore, P.; Nucara, A.; Cannavò, D.; De Marzi, G.; Calvani, P.; Marcelli, A.; Sussmann, R. S.; Whitehead, A. J.; Dodge, C. N.; Krehan, A. J.; et al. Infrared Properties of Chemical-Vapor Deposition Polycrystalline Diamond Windows. *Appl. Opt.* **1998**, *37*, 5731.
(7) Schädle, T.; Mizaikoff, B. Mid-Infrared Waveguides: A Perspective. *Appl. Spectrosc.* **2016**, *70*, 1625−1638.
(8) Plunkett, S. E.; Propst, S.; Braiman, M. S. Supported Planar Germanium Waveguides for Infrared Evanescent-Wave Sensing. *Appl. Opt.* **1997**, *36*, 4055.
(9) Chang, Y.-C.; Wägli, P.; Paeder, V.; Homsy, A.; Hvozdara, L.; van der Wal, P.; Di Francesco, J.; de Rooij, N. F.; Peter Herzig, H. Cocaine Detection by a Mid-Infrared Waveguide Integrated with a Microfluidic Chip. *Lab Chip* **2012**, *12*, 3020.
(10) Chang, Y.-C.; Paeder, V.; Hvozdara, L.; Hartmann, J.-M.; Herzig, H. P. Low-Loss Germanium Strip Waveguides on Silicon for the Mid-Infrared. *Opt. Lett.* **2012**, *37*, 2883.
(11) Soref, R. A.; Emelett, S. J.; Buchwald, W. R. Silicon Waveguided Components for the Long-Wave Infrared Region. *J. Opt. A: Pure Appl. Opt.* **2006**, *8*, 840−848.
(12) Liu, T.; Liu, P.; Zhang, L.; Zhou, Y.-F.; Yu, X.-F.; Zhao, J.-H.; Wang, X.-L. Visible and Near-Infrared Planar Waveguide Structure of Polycrystalline Zinc Sulfide from C Ions Implantation. *Opt. Express* **2013**, *21*, 4671.
(13) Mittal, V.; Sessions, N. P.; Wilkinson, J. S.; Murugan, G. S. Optical Quality ZnSe Films and Low Loss Waveguides on Si Substrates for Mid-Infrared Applications. *Opt. Mater. Express* **2017**, *7*, 712.
(14) Ma, P.; Choi, D.-Y.; Yu, Y.; Yang, Z.; Vu, K.; Nguyen, T.; Mitchell, A.; Luther-Davies, B.; Madden, S. High Q Factor Chalcogenide Ring Resonators for Cavity-Enhanced MIR Spectroscopic Sensing. *Opt. Express* **2015**, *23*, 19969.
(15) DeCorby, R. G.; Ponnampalam, N.; Pai, M. M.; Nguyen, H. T.; Dwivedi, P. K.; Clement, T. J.; Haugen, C. J.; McMullin, J. N.; Kasap, S. O. High Index Contrast Waveguides in Chalcogenide Glass and Polymer. *IEEE J. Sel. Top. Quantum Electron.* **2005**, *11*, 539−546.

DOI: 10.1021/acsomega.8b00623
ACS Omega 2018, 3, 6190−6198

(16) Smith, C. J.; Shankar, R.; Laderer, M.; Frish, M. B.; Loncar, M.; Allen, M. G. Sensing Nitrous Oxide with QCL-Coupled Silicon-on-Sapphire Ring Resonators. *Opt. Express* **2015**, *23*, 5491−5499.
(17) Sieger, M.; Balluff, F.; Wang, X.; Kim, S.-S.; Leidner, L.; Gauglitz, G.; Mizaikoff, B. On-Chip Integrated Mid-Infrared GaAs/AlGaAs Mach−Zehnder Interferometer. *Anal. Chem.* **2013**, *85*, 3050−3052.
(18) Leidner, L.; Ewald, M.; Sieger, M.; Mizaikoff, B.; Gauglitz, G. Migrating the Mach-Zehnder Chemical and Bio-Sensor to the Mid-Infrared Region. In *Proceedings of SPIE*; Baldini, F., Homola, J., Lieberman, R. A., Eds., 2013; Vol. *8774*, p 87740S.
(19) Wang, X.; Antoszewski, J.; Putrino, G.; Lei, W.; Faraone, L.; Mizaikoff, B. Mercury − Cadmium − Telluride Waveguides − A Novel Strategy for On-Chip Mid-Infrared Sensors. *Anal. Chem.* **2013**, *85*, 10648−10652.
(20) Rath, P.; Khasminskaya, S.; Nebel, C.; Wild, C.; Pernice, W. H. P. Diamond-Integrated Optomechanical Circuits. *Nat. Commun.* **2013**, *4*, 1690.
(21) Prajzler, V.; Varga, M.; Nekvindova, P.; Remes, Z.; Kromka, A. Design and Investigation of Properties of Nanocrystalline Diamond Optical Planar Waveguides. *Opt. Express* **2013**, *21*, 8417.
(22) López-Lorente, Á. I.; Wang, P.; Sieger, M.; Vargas Catalan, E.; Karlsson, M.; Nikolajeff, F.; Österlund, L.; Mizaikoff, B. Mid-Infrared Thin-Film Diamond Waveguides Combined with Tunable Quantum Cascade Lasers for Analyzing the Secondary Structure of Proteins. *Phys. Status Solidi A* **2016**, *213*, 2117−2123.
(23) Wang, X.; Karlsson, M.; Forsberg, P.; Sieger, M.; Nikolajeff, F.; Österlund, L.; Mizaikoff, B. Diamonds Are a Spectroscopist's Best Friend: Thin-Film Diamond Mid-Infrared Waveguides for Advanced Chemical Sensors/Biosensors. *Anal. Chem.* **2014**, *86*, 8136−8141.
(24) Malmström, M.; Karlsson, M.; Forsberg, P.; Cai, Y.; Nikolajeff, F.; Laurell, F. Waveguides in Polycrystalline Diamond for Mid-IR Sensing. *Opt. Mater. Express* **2016**, *6*, 1286.
(25) Luong, J. H. T.; Male, K. B.; Glennon, J. D. Boron-Doped Diamond Electrode: Synthesis, Characterization, Functionalization and Analytical Applications. *Analyst* **2009**, *134*, 1965−1979.
(26) Diamond Materials GmbH. *The CVD Diamond Booklet* [Online]; Fraunhofer IAF: Freiburg, 2018; p 4. http://www.diamond-materials.com/downloads/cvd_diamond_booklet.pdf (accessed April 20, 2018).
(27) Barjon, J.; Habka, N.; Mer, C.; Jomard, F.; Chevallier, J.; Bergonzo, P. Resistivity of Boron Doped Diamond. *Phys. Status Solidi RRL* **2009**, *3*, 202−204.
(28) Schreck, M.; Gsell, S.; Brescia, R.; Fischer, M. Ion Bombardment Induced Buried Lateral Growth: The Key Mechanism for the Synthesis of Single Crystal Diamond Wafers. *Sci. Rep.* **2017**, *7*, 44462.
(29) Nad, S.; Gu, Y.; Asmussen, J. Growth Strategies for Large and High Quality Single Crystal Diamond Substrates. *Diamond Relat. Mater.* **2015**, *60*, 26−34.
(30) Krishnan, R. S. Thermal Expansion of Diamond. *Nature* **1944**, *154*, 486−487.
(31) Watanabe, H.; Yamada, N.; Okaji, M. Linear Thermal Expansion Coefficient of Silicon from 293 to 1000 K. *Int. J. Thermophys.* **2004**, *25*, 221−236.
(32) Hidnert, P.; Gero, W. B. Thermal Expansion of Molybdenum. *Sci. Pap. Bur. Stand.* **1924**, *19*, 429−444.
(33) Sieger, M.; Kos, G.; Sulyok, M.; Godejohann, M.; Krska, R.; Mizaikoff, B. Portable Infrared Laser Spectroscopy for On-Site Mycotoxin Analysis. *Sci. Rep.* **2017**, *7*, 44028.
(34) Haas, J.; Stach, R.; Sieger, M.; Gashi, Z.; Godejohann, M.; Mizaikoff, B. Sensing Chlorinated Hydrocarbons via Miniaturized GaAs/AlGaAs Thin-Film Waveguide Flow Cells Coupled to Quantum Cascade Lasers. *Anal. Methods* **2016**, *8*, 6602−6606.
(35) Sieger, M.; Haas, J.; Jetter, M.; Michler, P.; Godejohann, M.; Mizaikoff, B. Mid-Infrared Spectroscopy Platform Based on GaAs/AlGaAs Thin-Film Waveguides and Quantum Cascade Lasers. *Anal. Chem.* **2016**, *88*, 2558−2562.
(36) Saleh, B. E. A.; Teich, M. C. Fiber Optics. *Fundamentals of Photonics*; John Wiley & Sons, Inc.: New York, 1991; Vol. *5*, pp 272−309.
(37) López-Lorente, Á. I.; Mizaikoff, B. Mid-Infrared Spectroscopy for Protein Analysis: Potential and Challenges. *Anal. Bioanal. Chem.* **2016**, *408*, 2875−2889.
(38) Lammer, A. Mechanical Properties of Polycrystalline Diamonds. *Mater. Sci. Technol.* **1988**, *4*, 949−955.
(39) Wang, X.; Kim, S.-S.; Roßbach, R.; Jetter, M.; Michler, P.; Mizaikoff, B. Ultra-Sensitive Mid-Infrared Evanescent Field Sensors Combining Thin-Film Strip Waveguides with Quantum Cascade Lasers. *Analyst* **2012**, *137*, 2322.
(40) Biliškov, N.; Baranović, G. Infrared Spectroscopy of Liquid Water−N,N-Dimethylformamide Mixtures. *J. Mol. Liq.* **2009**, *144*, 155−162.
(41) Kischkat, J.; Peters, S.; Gruska, B.; Semtsiv, M.; Chashnikova, M.; Klinkmüller, M.; Fedosenko, O.; Machulik, S.; Aleksandrova, A.; Monastyrskyi, G.; et al. Mid-Infrared Optical Properties of Thin Films of Aluminum Oxide, Titanium Dioxide, Silicon Dioxide, Aluminum Nitride, and Silicon Nitride. *Appl. Opt.* **2012**, *51*, 6789.
(42) Schroder, D. K.; Thomas, R. N.; Swartz, J. C. Free Carrier Absorption in Silicon. *IEEE Trans. Electron Devices* **1978**, *25*, 254−261.
(43) Chandler-Horowitz, D.; Amirtharaj, P. M. High-Accuracy, Midinfrared (450cm−1 ω 4000cm−1) Refractive Index Values of Silicon. *J. Appl. Phys.* **2005**, *97*, 123526.
(44) Forsberg, P.; Karlsson, M. Inclined Surfaces in Diamond: Broadband Antireflective Structures and Coupling Light through Waveguides. *Opt. Express* **2013**, *21*, 2693.
(45) Vargas Catalán, E.; Huby, E.; Forsberg, P.; Jolivet, A.; Baudoz, P.; Carlomagno, B.; Delacroix, C.; Habraken, S.; Mawet, D.; Surdej, J.; et al. Optimizing the Subwavelength Grating of L -Band Annular Groove Phase Masks for High Coronagraphic Performance. *Astron. Astrophys.* **2016**, *595*, A127.
(46) Delacroix, C.; Forsberg, P.; Karlsson, M.; Mawet, D.; Absil, O.; Hanot, C.; Surdej, J.; Habraken, S. Design, Manufacturing, and Performance Analysis of Mid-Infrared Achromatic Half-Wave Plates with Diamond Subwavelength Gratings. *Appl. Optic.* **2012**, *51*, 5897−5902.

DOI: 10.1021/acsomega.8b00623
ACS Omega 2018, 3, 6190−6198